J|A|C|S
ARTICLES

ARTICLES

Published on Web 07/24/2009

Fast Electron-Transfer Kinetics Probed in Nanofluidic Channels

Marcel A. G. Zevenbergen, Bernhard L. Wolfrum,[†] Edgar D. Goluch,
Pradyumna S. Singh, and Serge G. Lemay*

*Kavli Institute of Nanoscience, Delft University of Technology, Lorentzweg 1,
2628 CJ Delft, The Netherlands*

Received March 24, 2009; E-mail: s.g.lemay@tudelft.nl

Abstract: We demonstrate that a 50 nm high solution-filled cavity bounded by two parallel electrodes in which electrochemically active molecules undergo rapid redox cycling can be used to determine very fast electron-transfer kinetics. We illustrate this capability by showing that the heterogeneous rate constant of $Fc(MeOH)_2$ sensitively depends on the type and concentration of the supporting electrolyte. These solid-state devices are mechanically robust and stable over time and therefore have the potential to become a widespread and versatile tool for electrochemical measurements.

Introduction

Studying the heterogeneous electron-transfer kinetics of fast outer-sphere reactions by voltammetric methods represents a major experimental challenge. This is mainly because voltammetric measurements only become sensitive to heterogeneous kinetics when electron transfer rates and mass transport rates to the working electrode become comparable, which is difficult to achieve for fast reactions using conventional electrochemical instrumentation. This requirement has been achieved with fast voltammetry at microelectrodes,[1−3] scanning electrochemical microscopy (SECM),[4−6] and, most extensively in recent years, voltammetry with micro- or nanometer-sized electrodes.[7−16] The latter is extremely challenging because, despite advances in the

fabrication of nanoelectrodes, extracting rate constants from voltammetry data requires knowledge of the exact shape of each electrode. This information is often only accessible from indirect measurements combined with assumptions about the geometry.

Here we show that the electron-transfer kinetics for fast chemically reversible reactions can be determined using nanofluidic devices fabricated using lithographic methods. Our approach is illustrated in Figure 1a: two electrodes are embedded in a solution-filled channel that is several tens of nanometers high. Reversibly redox-active molecules situated in the region between the electrodes can be repeatedly oxidized and reduced, greatly enhancing the current. While it does not allow continuously tuning the electrode spacing as does SECM, this approach yields precise knowledge of and control over the electrode geometry. Furthermore, the devices are stable over time and multiple, essentially identical devices can be reproducibly fabricated, allowing for systematic studies. We illustrate this by showing that the standard heterogeneous rate constant k^0 for ferrocenedimethanol, $Fc(MeOH)_2$, depends sensitively on the composition of the supporting electrolyte.

Materials and Methods

Device Fabrication and Characterization. The fabrication scheme is illustrated in Figure 1b. In step 1, a 40 μm long, 1.5 μm wide, and 15 nm high platinum bottom electrode was first defined on a standard Si wafer with 500 nm thermally grown SiO_2. This was done by depositing a Pt layer using electron-beam evaporation and patterning it by electron-beam lithography and a polymethylmethacrylate (PMMA)-based lift-off process. With the same technique, a 33 μm long, 2 μm wide, and 60 or 50 nm high sputtered sacrificial layer of chromium was patterned (step 2). Its height was confirmed after deposition with a surface profiler (Tencor Alpha-Step 500). The Cr completely enveloped the bottom electrode, ensuring that there was no contact to the top electrode. In step 3, the top electrode consisting of a 10 μm long, 2.5 μm wide, and 60 nm high Pt layer was patterned on top of the Cr. The device was then passivated with a ~550 nm layer of sputtered SiO_2. In step 4, the final lithography step, two 1 μm^2 fluidic access holes to the sacrificial Cr layer were created by CHF_3/O_2 reactive ion etching. The devices used here had a designed electrode spacing of ~60

† Current address: IBN-2, Forschungszentrum Jülich GmbH, JARA-FIT, Germany.
(1) Howell, J. O.; Wightman, R. M. *Anal. Chem.* **1984**, *56*, 524–529.
(2) Wipf, D. O.; Kristensen, E. W.; Deakin, M. R.; Wightman, R. M. *Anal. Chem.* **1988**, *60*, 306–310.
(3) Montenegro, M. I.; Pletcher, D. *J. Electroanal. Chem.* **1986**, *200*, 371–374.
(4) Shao, Y. H.; Mirkin, M. V.; Fish, G.; Kokotov, S.; Palanker, D.; Lewis, A. *Anal. Chem.* **1997**, *69*, 1627–1634.
(5) Wipf, D. O.; Bard, A. J. *J. Electrochem. Soc.* **1991**, *138*, 469–474.
(6) Mirkin, M. V.; Richards, T. C.; Bard, A. J. *J. Phys. Chem.* **1993**, *97*, 7672–7677.
(7) Watkins, J. J.; Chen, J. Y.; White, H. S.; Abruna, H. D.; Maisonhaute, E.; Amatore, C. *Anal. Chem.* **2003**, *75*, 3962–3971.
(8) Russell, A.; Repka, K.; Dibble, T.; Ghoroghchian, J.; Smith, J. J.; Fleischmann, M.; Pitt, C. H.; Pons, S. *Anal. Chem.* **1986**, *58*, 2961–2964.
(9) Penner, R. M.; Heben, M. J.; Longin, T. L.; Lewis, N. S. *Science* **1990**, *250*, 1118–1121.
(10) Bond, A. M.; Henderson, T. L. E.; Mann, D. R.; Mann, T. F.; Thormann, W.; Zoski, C. G. *Anal. Chem.* **1988**, *60*, 1878–1882.
(11) Sun, P.; Mirkin, M. V. *Anal. Chem.* **2006**, *78*, 6526–6534.
(12) Watkins, J. J.; White, H. S. *Langmuir* **2004**, *20*, 5474–5483.
(13) Chen, S. L.; Kucernak, A. *J. Phys. Chem. B* **2002**, *106*, 9396–9404.
(14) Slevin, C. J.; Gray, N. J.; Macpherson, J. V.; Webb, M. A.; Unwin, P. R. *Electrochem. Commun.* **1999**, *1*, 282–288.
(15) Heller, I.; Kong, J.; Heering, H. A.; Williams, K. A.; Lemay, S. G.; Dekker, C. *Nano Lett.* **2005**, *5*, 137–142.
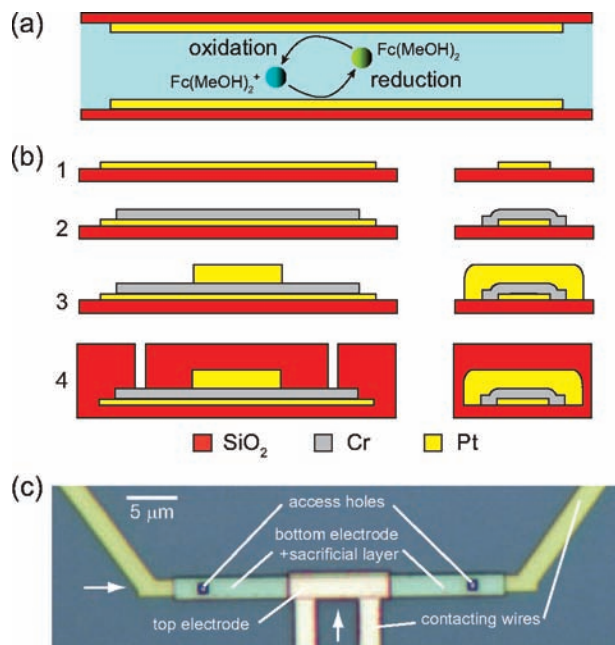(16) Velmurugan, J.; Sun, P.; Mirkin, M. V. *J. Phys. Chem. C* **2009**, *113*, 459–464.

10.1021/ja902331u CCC: $40.75 © 2009 American Chemical Society

J. AM. CHEM. SOC. 2009, *131*, 11471–11477 ■ **11471**

Figure 1. (a) Schematic illustration of redox cycling. (b) Device cross-sections at the four stages of the fabrication process, as would be obtained by cutting open the device and imaging the exposed surface. The cross-sections in the left and right column correspond to the long and short axis of the device, respectively. These sketches are not drawn to scale: in particular, the thickness of the Cr layer was stretched ∼25 times for clarity. 1. On an insulating wafer the bottom Pt electrode is patterned and deposited. 2. A Cr sacrificial layer is deposited that ultimately determines the height of the channel. 3. The top Pt electrode is patterned and deposited. 4. A SiO$_2$ capping layer is sputtered and two access holes are etched that serve as entrances for fluid. (c) Microscope image of a finished device prior to the sacrificial chromium etch. The device is seen from above. The arrows indicate the lines along which the schematic cross-sections of part b are shown (horizontal arrow: left column, vertical arrow: right column).

Figure 2. Current flowing between top and bottom electrodes as a function of time during the sacrificial chromium layer etch. A small bias of 10 mV was applied between the electrodes. As the etch proceeded, the current diminished. Eventually, when all the Cr had been etched, contact was lost between the two electrodes.

nm or ∼50 nm, as determined by the thickness of the Cr layer, while the region of overlap between the two electrodes, the "active region" of the device, had an area of 10 μm × 1.5 μm. Figure 1c shows an optical image of such a device prior to Cr etching. At this stage of fabrication, the devices are extremely robust and can be stored indefinitely without fear of contamination because the electrodes are not exposed to the environment. Finally, the sacrificial Cr layer was selectively etched by immersing the device in chromium etchant,[17] creating a cavity for fluid.

The chromium etch progress could be monitored optically or electrically. Prior to etching, the Cr layer provided an electrical connection between the top and bottom electrode. By applying a small bias (10 mV) between the top and bottom electrode and measuring the resulting current, the sacrificial layer etch could be monitored in real time, as illustrated in Figure 2. As the etch proceeded, the current decreased until eventually enough chromium had been etched that the electrical contact was broken. The device remained in the Cr etchant for at least an additional 15 min to ensure that all of the Cr was removed. Afterward, the device was cleaned by rinsing extensively with deionized water and subsequently filled with 0.5 M H$_2$SO$_4$ aqueous solution. The potential of both electrodes was swept between −0.15 and 1.15 V vs Ag/AgCl at least 20 cycles, and the characteristic behavior of Pt in sulfuric acid was observed (cyclic voltammograms are shown in the Supporting Information).

The spacing between the two Pt electrodes was controlled very precisely by tuning the thickness of the Cr layer. In order to quantify the electrode roughness, the root-mean-square variation of the height
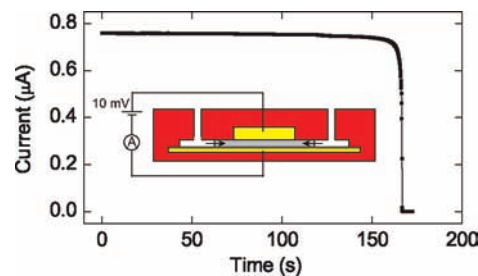
of the deposited films was determined by atomic force microscopy (AFM). The rms roughness was 0.45 and 1.05 nm for the bottom and top electrodes, respectively (images are provided in the Supporting Information). The residual roughness of both electrode surfaces is thus much smaller than the electrode spacing and is expected to be inconsequential.

To verify that no Cr remained, we performed two element-sensitive characterization experiments. First, energy-dispersive X-ray spectroscopy (EDS) was performed on test samples that contained layers of platinum and chromium (15 nm Pt, 60 nm Cr), similar to those used in the fluidic devices. After chromium etching was performed, the Cr signature in the EDS spectrum completely disappeared (spectra shown in the Supporting Information). EDS, however, cannot resolve (sub)monolayers of Cr residues. Therefore X-ray photoelectron spectroscopy (XPS) was performed on a SiO$_2$ wafer on which 15 nm Pt followed by 1 nm Cr had been evaporated. The Cr could be clearly resolved before the etching process (20.6 atom percent) while after, the Cr signal dropped below the detection limit of the instrument of 0.3 atom percent. This strongly suggests that the etching protocol leaves behind no Cr residues of consequence. Further details are provided in the Supporting Information.

Electrical Measurements and Chemicals. Cyclic voltammograms were recorded with two Keithley 6430 subfemtoamp remote sourcemeters (Keithley Instruments) that were controlled with in-house Labview software (data of Figure 4) or with a CHI832B bipotentiostat (CH Instruments, data of Figure 5). The quiet time of the bipotentiostat was set to 5 s. All cyclic voltammograms started with the forward (low potential to high potential) sweep. A standard Ag/AgCl electrode (3 M NaCl, BASi) that served both as a reference and a counter electrode was immersed in a PDMS reservoir that contacted the device.

Ferrocenedimethanol, Fc(MeOH)$_2$, was purchased from Acros (cat. no. 382250010), while sodium perchlorate, NaClO$_4$, and potassium chloride, KCl, were purchased from Sigma-Aldrich (cat. no. 410241 and P3911, respectively). The chromium etchant (Selectipur) was from BASF and the sulfuric acid, H$_2$SO$_4$, from J. T. Baker (cat. no. 6057). All the solutions were prepared in 18.2 MΩ cm deionized water (Millipore).

Theory

The small electrode spacing leads to very efficient mass transport: the current density over the full 15 μm^2 surface of our electrodes is equivalent to that at a 0.016 μm^2 hemispherical electrode. This allows the influence of the finite electron-transfer rate to be determined even for fast reactions. In this section, we derive an expression for the current as a function of the applied potential to both the top and bottom electrode where electron-transfer kinetics are described by Butler−Volmer kinetics. We also introduce an alternate way of extracting the heterogeneous rate constant k^0 by comparing the steady-state current wave height for two cases: first, when an oxidizing

(17) Sparreboom, W.; Eijkel, J. C. T.; Bomer, J.; van den Berg, A. *Lab Chip* **2008**, *8*, 402–407.
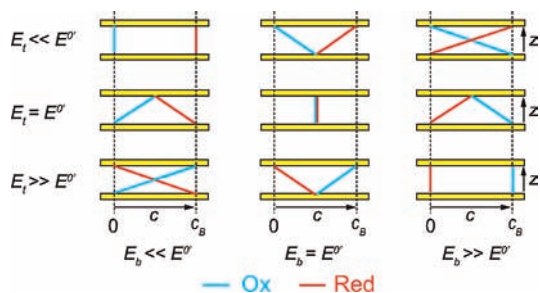
Figure 3. Schematic diagram of the linear concentration profiles across the channel for various potentials E_t and E_b applied to the top and bottom electrodes, respectively. Fc(MeOH)$_2$ can be in its oxidized (blue lines) or reduced form (red lines). The total concentration of the redox species (oxidized and reduced) equals the bulk Fc(MeOH)$_2$ concentration c_B. $E_t \ll E^{0\prime}$, $E_t = E^{0\prime}$ and $E_t \gg E^{0\prime}$ corresponds to the top electrode being biased at a highly reducing overpotential, at the formal potential, and at a highly oxidating overpotential, respectively.

potential is applied to one electrode while the potential of the other electrode is swept, and, second, when the formal potential is applied to the first electrode. These currents differ because when the formal potential is applied to one electrode, the total current remains electron-transfer limited even when a large overpotential is applied to the other electrode.

Steady state is approached in a characteristic time $\tau = z^2/2D$, where z is the height of cavity and D is the diffusion coefficient. Because τ is of the order of microseconds, which is very short on the time scale of our measurements, we can assume that the redox species concentration profile inside the device is in steady state. This yields linear concentration profiles (illustrated in Figure 3) that are similar to the concentration profiles of classic thin-layer cells[18,19] and SECM in variable substrate potential mode.[20] Because the electrode spacing is several tens of nanometers, the concentration gradients are very steep, resulting in the rate of mass transfer being ~40 times higher. Also, our geometry ensures that ionic fluxes are essentially uniform over the surface of the electrodes during redox cycling, simplifying interpretation. Even smaller electrode distances were developed recently in closed thin-layer cells.[21] One difference is that here the device is connected to a reservoir; the solution being probed can therefore readily be substituted during measurements, allowing a systematic study of different supporting electrolytes.

The device is filled with water containing a total concentration c_B of ferrocenedimethanol that can be found in its oxidized or reduced form. Let $c_{t,o}$, $c_{t,r}$, $c_{b,o}$, and $c_{b,r}$ be the concentrations of oxidized and reduced ferrocenedimethanol at the top and bottom electrodes, respectively. We assume for simplicity that the diffusion coefficient D is the same for the oxidized and reduced forms. We also ignore mass transport between the electrode region and the bulk reservoir in calculating ionic fluxes; doing so introduces a negligible error <1% of the typical redox cycling currents.[22,23] The linear concentration profiles in the cavity, with fluxes j_o and j_r of oxidized and reduced species, respectively, are given by

(18) Reilley, C. N. *Rev. Pure Appl. Chem.* **1968**, *18*, 137–151.
(19) Anderson, L. B.; Reilley, C. N. *J. Electroanal. Chem.* **1965**, *10*, 295–305.
(20) Zoski, C. G.; Luman, C. R.; Fernandez, J. L.; Bard, A. *J. Anal. Chem.* **2007**, *79*, 4957–4966.
(21) Sun, P.; Mirkin, M. V. *J. Am. Chem. Soc.* **2008**, *130*, 8241–8250.
(22) Zevenbergen, M. A. G.; Krapf, D.; Zuiddam, M. R.; Lemay, S. G. *Nano Lett.* **2007**, *7*, 384–388.
(23) Wolfrum, B.; Zevenbergen, M.; Lemay, S. *Anal. Chem.* **2008**, *80*, 972–977.

$$j_o = D\left(\frac{c_{b,o} - c_{t,o}}{z}\right), \quad j_r = D\left(\frac{c_{b,r} - c_{t,r}}{z}\right) \quad (1)$$

Here we introduced the convention that positive fluxes and electrical currents flow from the bottom electrode to the top electrode. The concentrations $c_{t,o}$, $c_{t,r}$, $c_{b,o}$, and $c_{b,r}$ are not mutually independent. First, mass conservation implies that

$$i = FAj_o = -FAj_r \quad (2)$$

where i is the steady-state redox cycling current, A the area where the electrodes overlap (15 μm^2), and F Faraday's constant. Second, the total number of molecules in the device (in oxidized or reduced form) corresponds to the number given by the bulk concentration c_B. Integration of the concentration profile thus yields

$$\frac{c_{b,o} + c_{t,o}}{2} + \frac{c_{b,r} + c_{t,r}}{2} = c_B \quad (3)$$

Third, we describe heterogeneous electron transfer at the top and bottom electrodes using Butler–Volmer kinetics,

$$\frac{i}{FA} = k^0 c_{b,r} e^{(1-\alpha)f\eta_b} - k^0 c_{b,o} e^{-\alpha f\eta_b}$$
$$= -(k^0 c_{t,r} e^{(1-\alpha)f\eta_t} - k^0 c_{t,o} e^{-\alpha f\eta_t}) \quad (4)$$

Here k^0 is the heterogeneous rate constant, α the transfer coefficient, $\eta_{t,b} = E_{t,b} - E^{0\prime}$ the overpotential applied to the top and bottom electrodes, respectively, $E^{0\prime}$ the formal potential, and $f = F/RT$ with R the gas constant and T the temperature. Combining eqs 1–4 yields an expression for the current,

$$i = \frac{i_{lim}\left(\dfrac{e^{f\eta_b}}{1 + e^{f\eta_b}} - \dfrac{e^{f\eta_t}}{1 + e^{f\eta_t}}\right)}{1 + \dfrac{D}{zk^0}\left(\dfrac{e^{\alpha f\eta_b}}{1 + e^{f\eta_b}} + \dfrac{e^{\alpha f\eta_t}}{1 + e^{f\eta_t}}\right)} \quad (5)$$

Here i_{lim} is the diffusion-limited current given by

$$i_{lim} = \frac{nFADc_B}{z} \quad (6)$$

where n is the number of electrons transferred per molecule ($n = 1$ for Fc(MeOH)$_2$). For the case $E_t \ll E^{0\prime}$, eq 5 reduces to

$$i = \frac{i_{lim}}{1 + e^{-f\eta_b} + \dfrac{D}{zk^0}e^{-(1-\alpha)f\eta_b}} \quad (7)$$

This expression is the thin-layer-cell analogue to the standard Butler–Volmer (BV) expression for an oxidation reaction at an ultramicroelectrode. Note that the dimensionless rate constant D/zk^0 depends on the distance z between the electrodes while the diffusion-limited current depends on both z and the area A. This allows independently tuning the rate of mass transport and the magnitude of the total current.

We now compare the maximum currents for two different cases. First, consider the case where a large reductive overpotential is applied to the top electrode, $e^{f\eta_t} \ll 1$. When the potential of the bottom electrode is varied from a reductive potential $e^{f\eta_b} \ll 1$ to an oxidative potential $e^{f\eta_b} \gg 1$, eq 7 indicates that the current varies between a minimum of 0 and a maximum of i_{lim}, yielding a wave height $\Delta i(E_t \ll E^{0\prime}) = i_{lim}$.

Second, consider the case where the formal potential is applied to the top electrode, $E_t = E^{0\prime}$. Upon cycling the bottom electrode, eq 5 indicates that the current varies between $i = -i_{lim}/2(1 + D/2zk^0)$ for $e^{f\eta_t} \ll 1$ and $i = +i_{lim}/2(1 + D/2zk^0)$ for $e^{f\eta_t} \gg 1$. The corresponding wave height is $\Delta i(E_t = E^{0\prime}) = i_{lim}/(1 + D/2zk^0)$. The ratio of the wave heights in these two cases is thus

$$\frac{\Delta i(E_t = E^{0\prime})}{\Delta i(E_t \ll E^{0\prime})} = \frac{1}{1 + D/2zk^0} \quad (8)$$

This ratio is always ≤ 1 and approaches unity as the voltammogram becomes Nernstian. This result reflects the fact that even when a large overpotential is applied to the bottom electrode, the total measured current remains electron-transfer limited when the formal potential is applied to the top electrode.

Results

Current Amplification by Redox Cycling. Figure 4 illustrates the basic functioning of the device through cyclic voltammograms obtained under various biasing conditions. These voltammograms are for a device with a designed channel height ~ 60 nm (based on the thickness of the Cr layer) and filled with an aqueous solution of 1.2 ± 0.1 mM $Fc(MeOH)_2$ and 2 M KCl as supporting electrolyte. We also added 5 mM H_2SO_4 to prevent the electrodes from fouling during extended measurements.

The voltammogram in Figure 4a was obtained by sweeping the potential of the bottom electrode, E_b, while the top electrode was disconnected. The current (black line) reached a steady-state diffusion-limited plateau, i_{lim}, of 120 pA at high overpotential. In this case, redox cycling could not occur and the current was therefore limited by the rate of mass transport from the bulk solution to the bottom electrode via the entrance holes. In order to estimate the magnitude of the diffusion-limited flux expected from theory, we have performed finite element calculations (Comsol Multiphysics 3.4) using a three-dimensional geometry model of our device (figures and details are provided in the Supporting Information). These calculations yielded a diffusion-limited current of 150 pA without fitting parameters, in reasonable agreement with the measured current given the complex three-dimensional geometry of the entrance hole.

Figure 4b shows a voltammogram for which the potential of the top electrode, E_t, was swept while the bottom electrode was disconnected (red line). The recorded voltammogram is remarkably similar to the voltammogram of Figure 4a despite the asymmetrical geometry of the device (in particular, the distance from the edges of the top electrode to the entrance holes is 8 μm while the bottom electrode extends throughout the entire channel). This behavior is however easily understood: when an oxidizing potential is applied to the top electrode, $Fc(MeOH)_2$ in the channel is almost completely oxidized while the reduced form is depleted. Since the (floating) bottom electrode is in equilibrium with the electroactive species, its potential approaches the Nernst potential of the solution inside the cavity. This induced oxidizing potential allows oxidation of reduced species near the entrance holes and thus leads to the same i_{lim} as if an oxidizing potential was applied to this electrode. This
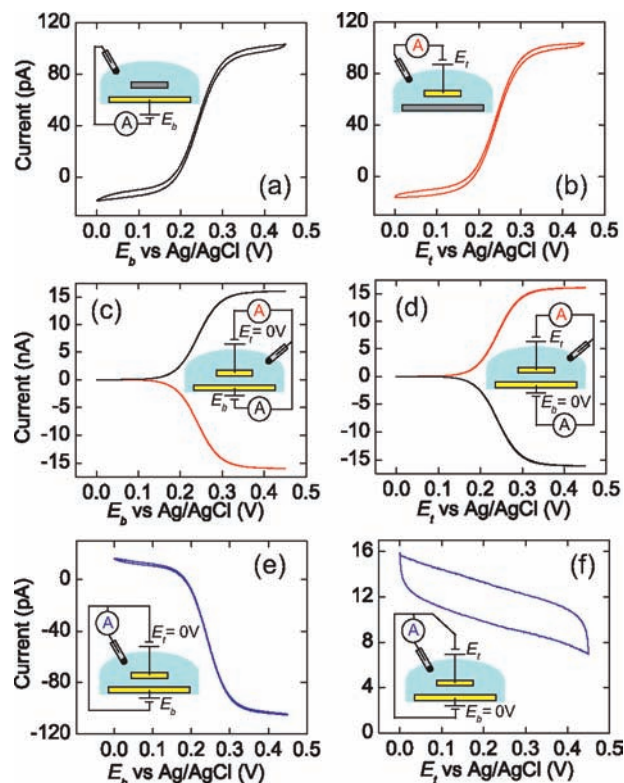

Figure 4. Cyclic voltammograms of 1.2 mM $Fc(MeOH)_2$ in 2 M KCl (scan rate 5 mV/s). Black, red, and blue lines represent the current through the bottom, top, and reference electrode, respectively. The insets show a schematic diagram of the wiring. (a) The potential of the bottom electrode E_b was swept while the potential of the top electrode E_t was left floating. The current reached a steady-state plateau i_{lim} of 120 pA that is limited by mass transfer from the bulk solution via the entrance holes. (b) E_t was cycled while E_b was left floating. i_{lim} is essentially the same as for part a. This is because an oxidizing potential was induced on the floating bottom electrode, as discussed in the text. (c) E_b was varied while $E_t = 0$ V. Redox cycling amplified i_{lim} to 16.3 nA. The current through the top electrode has the opposite sign as in part b because a reducing instead of an oxidizing potential was applied to this electrode. (d) Inverting the role of the electrodes (E_t cycled while $E_b = 0$ V) yielded identical (but inverted) voltammograms as in part c. (e) Current through the reference electrode i_{ref} in redox cycling mode (E_b was cycled while $E_t = 0$ V). The voltammogram is essentially the inverse of part a. (f) i_{ref} when E_t was varied with $E_b = 0$ V. No faradaic current was observed at the reference electrode because the reducing potential of the (much larger) bottom electrode ensured that essentially no molecule could escape from the channel in oxidized form.

effect is analogous to the positive feedback observed in SECM when a tip approaches an unbiased conducting substrate.[5,24-27]

In Figure 4c, a cyclic voltammogram is shown when a reducing potential was applied to the top electrode ($E_t = 0$ V) and the bottom electrode was swept. A giant amplification of the current was observed due to redox cycling. In this case i_{lim} is determined by the one-dimensional diffusion profile between the two electrodes and is given by eq 6. Finite element calculations (shown in the Supporting Information) indicate that the slight fringing of the concentration profile near the electrode edge introduces a deviation of 0.6% and can therefore be

(24) Selzer, Y.; Turyan, I.; Mandler, D. *J. Phys. Chem. B* **1999**, *103*, 1509–1517.
(25) Xiong, H.; Guo, J. D.; Amemiya, S. *Anal. Chem.* **2007**, *79*, 2735–2744.
(26) Zoski, C. G.; Simjee, N.; Guenat, O.; Koudelka-Hep, M. *Anal. Chem.* **2004**, *76*, 62–72.
(27) Macpherson, J. V.; Slevin, C. J.; Unwin, P. R. *J. Chem. Soc., Faraday Trans.* **1996**, *92*, 3799–3805.

neglected. From the measured $i_{lim} = 16.3 \pm 0.1$ nA we extract[28] $z = 71 \pm 6$ nm, in approximate agreement with the fabricated spacing of 60 nm. We attribute the discrepancy to a slight upward buckling of the top electrode after the chromium has been etched.[22] The current through the top electrode (red line) was the inverse of that through the bottom electrode, demonstrating an essentially 100% cycling efficiency. Switching the role of the electrodes (E_t swept, E_b held fixed at 0 V) resulted as expected in identical, but inverted, voltammograms (Figure 4d).

Devices based on redox cycling such as interdigitated electrode arrays and thin-layer cells,[29−33] are often characterized by their so-called amplification factor. This quantity is defined as the ratio of the redox cycling current to the current flowing through the reference electrode or counter electrode, i_{ref}. Figure 4e,f shows measurements of i_{ref} under redox cycling conditions (blue lines). For the case when E_b was varied and $E_t = 0$ V (Figure 4e), a wave with amplitude −120 pA was observed. This signal was the inverse of the current that was observed when E_b was varied while the top electrode was left floating (Figure 4a). This was expected because this current originates from reduced molecules that diffuse from the bulk reservoir through the entrance holes and are oxidized at the bottom electrode near the entrance holes. The amplification factor in this case is therefore ∼136 (16.3 nA/120 pA).

When E_t was varied with $E_b = 0$ V (Figure 4f), no measurable faradaic current was observed in i_{ref}. Since the bottom electrode was now held at a reducing potential, each molecule that escaped the active area of the device in its oxidized form was reduced at the bottom electrode before it could leave the channel and reach the bulk. This led to such a small current to the reference electrode that it was completely masked by the background capacitive current. We estimate an upper bound for the faradaic current of ∼1 pA in this case, corresponding to an amplification factor >16000. This is the highest amplification factor ever reported for devices based on redox cycling.

For both cases in Figure 4e,f, the simultaneous measured redox cycling current was indistinguishable from the voltammograms in Figure 4c,d (data not shown). The low current levels measured for i_{ref} directly confirm that a separate counter electrode is not required in these measurements.

Ohmic Drops. Although the currents flowing through the reference electrode are small, the uncompensated resistance of the channel can be quite substantial. This is especially true for the top electrode, which is buried deep inside the device. In this section, we estimate upper bounds for the ohmic drops ΔE that can occur during our measurements. We find that $\Delta E \ll 1$ mV in all cases, indicating that ohmic drops can be safely ignored.

When an oxidizing potential is applied to the bottom electrode, an upper bound for the ohmic drop is given by the current to the reference electrode i_{ref} times the uncompensated resistance R_u of the current pathway. As was shown in the previous section, the highest measured value of i_{ref} in our experiments is 120 pA. R_u is approximately the resistance of the access hole, R_a, in series with the resistance of the bulk reservoir, R_r. The simple rectangular geometry of the access holes yields $R_a = l/\kappa d^2$, where $l = 550$ nm is the depth of the access hole, $d = 1$ μm is its width, and κ is the conductivity of the solution. R_r is dominated by the spreading resistance in the vicinity of the entrance hole and is given approximately by $R_r = 1/2\kappa d$ We use the conductivity of 250 mM sodium perchlorate, NaClO$_4$ ($\kappa = 24.7$ mS/cm),[34] because this is the most resistive solution employed in our experiments. For this case $R_u = 0.22$ MΩ and $R_r = 0.20$ MΩ, resulting in a maximum ohmic drop $\Delta E = 0.42$ M$\Omega \times$ 120 pA /2 $= 0.025$ mV (the factor 2 appears because there are two access holes).

For the top electrode, R_u is determined by $R_u = R_a + R_r + R_c$ where R_c is the resistance of the part of the channel from the access hole to the edge of the top electrode with length 8 μm. $R_c = 8$ μm/(24.7 mS/cm $\times$ 71 nm $\times$ 2 μm) $= 23$ MΩ and therefore dominates the resistance experienced by the top electrode. i_{ref} for this case is however <1 pA, resulting in an ohmic drop $\Delta E < 0.011$ mV.

In redox cycling mode, the current density inside the channel can become very high. This current only flows locally between the top and bottom electrodes, however, and in particular does not flow to the reference electrode. The resistance for this pathway is given by $R_z = z/A\kappa$, where $z = 71$ nm and $A = 15$ μm^2 are the height of the cavity and the area of overlap between the electrodes, respectively, as defined previously. This gives a resistance $R_z = 2$ kΩ and an upper bound for the potential drop in the solution between the electrodes of 16 nA $\times$ 2 kΩ $=$ 0.03 mV, which is completely negligible. Furthermore, this calculation grossly overestimates the actual potential drop because mass transport between the two electrodes is predominantly diffusive rather than electrokinetically driven as was assumed here.

Electron-Transfer Kinetics. Figure 5 shows cyclic voltammograms obtained for a device (designed height ∼50 nm) filled with 219 μM Fc(MeOH)$_2$, 250 mM KCl as supporting electrolyte, and 5 mM H$_2$SO$_4$. The voltammograms were obtained by cycling the potential of the bottom electrode, E_b, while the potential of the top electrode, E_t, was held constant at 0.05 V (reductive potential), 0.251 V (formal potential of Fc(MeOH)$_2$, $E^{0\prime}$), or 0.55 V (oxidative potential). In all cases the current through the bottom electrode (solid lines) was essentially the inverse of that through the top electrode (dashed lines) due to redox cycling. From the measured $i_{lim} = 4.02 \pm 0.02$ nA we extract $z = 53 \pm 3$ nm, in agreement with the fabricated spacing for this device.

To extract kinetic information, both forward and backward traces of the voltammograms were fitted separately with the BV equation (eq 7). The fitting parameters were i_{lim}, k^0, and α, the transfer coefficient. The value of $E^{0\prime}$ was independently determined for each solution as the value of E_t for which the voltammogram was exactly centered around the zero-current baseline (red curves in Figure 5). The resulting values of $E^{0\prime}$ are listed in Table 1; these values agreed within 1 mV with the half-wave potential measured in the same solution using a 10

(28) $D = 6.7 \pm 0.2 \times 10^{-10}$ m^2/s for 250 mM, 2 M KCl and 250 mM NaClO$_4$ solutions, and $6.5 \pm 0.2 \times 10^{-10}$ m^2/s for 2 M NaClO$_4$ solution, as derived from the steady state current at a 5 ± 0.1 μm radius Pt disk electrode (BASi, MF-2005).

(29) Rubinstein, I. *Physical electrochemistry: principles, methods and applications*; Marcel Dekker: New York, 1995.

(30) Ueno, K.; Hayashida, M.; Ye, J. Y.; Misawa, H. *Electrochem. Commun.* **2005**, *7*, 161–165.

(31) Paixao, T.; Richter, E. M.; Brito-Neto, J. G. A.; Bertotti, M. *Electrochem. Commun.* **2006**, *8*, 9–14.

(32) Ito, T.; Maruyama, K.; Sobue, K.; Ohya, S.; Niwa, O.; Suzuki, K. *Electroanalysis* **2004**, *16*, 2035–2041.

(33) Dam, V. A. T.; Olthuis, W.; van den Berg, A. *Analyst* **2007**, *132*, 365–370.

(34) Lide, D. R. *CRC Handbook of Chemistry and Physics*, 89th ed. (internet version 2009); CRC Press/Taylor and Francis: Boca Raton, 2009.
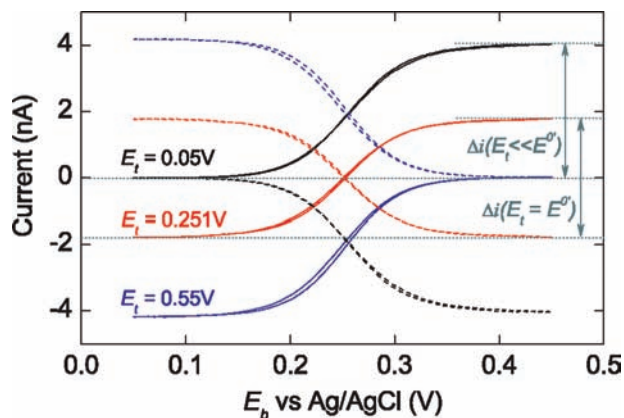
Figure 5. Cyclic voltammograms of 219 μM Fc(MeOH)$_2$ in 250 mM KCl (scan rate 10 mV/s). The potential of the bottom electrode E_b was varied between 0.05 and 0.45 V while the top electrode was held at 0.05 V (black curves), 0.251 V (red curves), and 0.55 V (blue curves). The solid and dashed curves represent the current through the bottom and the top electrode, respectively.

Table 1. Kinetic Parameters of Fc(MeOH)$_2$ in Different Electrolytes

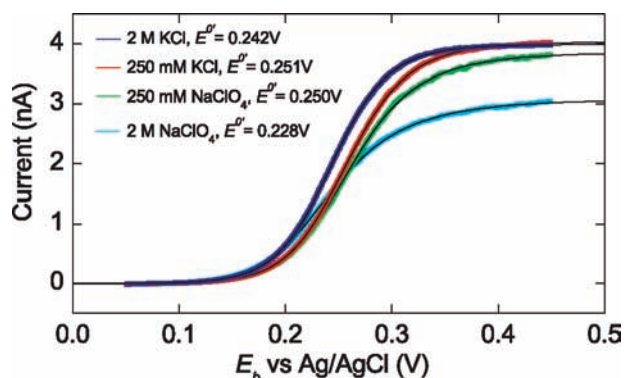| supporting electrolyte	250 mM KCl	2 M KCl	250 mM NaClO$_4$	2 M NaClO$_4$
$E^{0\prime}$ (V)	0.251	0.242	0.250	0.228
i_{lim} (nA)	4.02 ± 0.02	4.02 ± 0.02	3.78 ± 0.07	3.04 ± 0.02
α	0.49 ± 0.09	0.49 ± 0.13	0.56 ± 0.07	0.55 ± 0.04
k^0 (cm/s) BV fit	6.0 ± 1.4	15 ± 3[1]	3.2 ± 0.5	1.5 ± 0.2
$(\Delta i(E_t = E^{0\prime}))/$ $(\Delta i(E_t \ll E^{0\prime}))$	0.89 ± 0.01	0.94 ± 0.01	0.72 ± 0.02	0.74 ± 0.01
k^0 (cm/s) from eq 8	5.1 ± 0.6	10 ± 2	1.6 ± 0.2	1.7 ± 0.2

[1] Or >13 cm/s, as discussed in the text.

Figure 6. Cyclic voltammograms of 219 μM Fc(MeOH)$_2$ in various supporting salt solutions (scan rate 10 mV/s). E_b was varied while $E_t =$ 0.05 V. The solid lines are fits to the Butler–Volmer formalism, eq 7.

μm diameter Pt disk ultramicroelectrode (BASi MF-2005). We find that it is essential not to treat $E^{0\prime}$ as a free parameter in the fits as doing so leads to an insufficiently constrained fit that can easily converge to the wrong value of $E^{0\prime}$.

Voltammograms were recorded in different supporting electrolytes (2 M and 250 mM KCl and NaClO$_4$). Representative voltammograms and fits are shown in Figure 6. The fitted values are summarized in Table 1; the error bars represent the standard deviation in the values obtained from fits to 16 separate traces measured at two or more different times. All of the data shown here were obtained with a single device; measurements on additional devices yielded equivalent results. The shape of the voltammograms was independent of the order in which they were measured, and returning to a solution measured earlier recovered the earlier results.

As discussed in the Theory section, the thin-layer allows a second way of extracting k^0 by comparing the steady-state current wave height for the cases $E_t = E^{0\prime}$ and $E_t \ll E^{0\prime}$. It can be observed directly from inspection of Figure 5 (gray arrows) that the wave height is smaller in the case $E_t = E^{0\prime}$. This is expected because heterogeneous kinetics limit the current at the top electrode when $E_t = E^{0\prime}$. The heterogeneous rate constant can be extracted from the ratio of these currents, as given by eq 8, because D and z are known. For example, the measured ratio in Figure 5 was 0.89 ± 0.01, yielding $k^0 = 5.1 \pm 0.6$ cm/s. The ratios and k^0 obtained for the other supporting electrolytes are given in Table 1.

Discussion

Figure 6 indicates that the shape of the voltammograms strongly depends on supporting electrolyte. All of the voltammograms could be fitted quite well with eq 7 (BV equation), although a slight systematic deviation at large E_b was observed with 250 mM NaClO$_4$ (visible as a slightly different slope between the fit and the data at $E_b = 0.4$ V in Figure 6). The different voltammogram shapes are reflected in variations of the parameters $E^{0\prime}$, k^0, and i_{lim} with supporting electrolyte in Table 1. We discuss each of these parameters in turn.

We observed shifts in the formal potential $E^{0\prime}$ of −9 mV for KCl and −22 mV for NaClO$_4$ upon increasing the salt concentration from 250 mM to 2 M. The dependence of the formal potential on the activity coefficients for the reduced and oxidized species, γ_r and γ_o, is given by $E^{0\prime} = E^0 + (RT/F) \ln (\gamma_o/\gamma_r)$, where E^0 is the standard potential. Because the oxidized form of Fc(MeOH)$_2$ is charged, γ_o depends on the concentration of the supporting electrolyte. We estimate this dependence using the extended Debye–Hückel equation, $kT \ln \gamma_{o,r} = -z_{o,r}^2 e^2/ 8\pi\lambda\varepsilon(1 + \kappa a)$.[35] Here $z_{o,r}$ is the charge of the oxidized, reduced species, $-e$ the electron charge, λ the Debye length, ε the dielectric constant, and a the radius of the molecules (estimated at 0.3 nm, the approximate radius of ferrocene obtained from crystallography[36]). These equations predict a shift in the formal potential of −8 mV. The sign and magnitude of this prediction are consistent with the observations, suggesting that the shift is simply the result of changes in activity. A more quantitative, species-specific comparison is, however, not possible because extended Debye–Hückel theory ignores the finite size and structure of the ions and is expected to start breaking down at high concentrations of supporting electrolyte. Because these shifts were also observed at a standard UME, however, they are not a consequence of redox cycling and we do not discuss them further here.

Table 1 also reveals that the heterogeneous rate constant k^0 depends on the supporting electrolyte. Interestingly, the observed values of k^0 for different electrolytes span the whole range of previously reported values for ferrocene derivatives.[2,6−11,15,16] The highest k^0 (15 ± 3 cm/s) was observed in 2 M KCl. As a rule of thumb, kinetic information can only be extracted from fits to cyclic voltammograms when $D/zk^0 > 0.1$, which corresponds to $k^0 < 13$ cm/s for a device with $z = 53$ nm. This is reflected in the larger uncertainty in k^0 for this electrolyte. Following this rule of thumb, we can only conclude from the present experiment that $k^0 > 13$ cm/s in 2 M KCl.

(35) Lyklema, J. *Fundamentals of Interface and Colloid Science Volume 1: Fundamentals*; Academic Press: London, 1991.
(36) Takusagawa, F.; Koetzle, T. F. *Acta Crystallogr., Sect. B: Struct. Sci.* **1979**, *35*, 1074–1081.

The values of k^0 were determined using both fits to BV and using the alternate method given by eq 8. Both methods agree within statistical error, except for the 250 mM $NaClO_4$ result. Discrepancies between the two methods reflect the slight departure from ideality of the wave shape for $NaClO_4$. As discussed further below, this may originate from potential-induced changes or adsorption to the electrode (because the potential applied to the top electrode is different for the two methods, $E_t = 0.05$ V or $E_t = E^{0\prime}$, and the Frumkin correction may therefore differ in the two cases). We conclude that, while eq 8 provides a simple way of estimating the value of k^0, a full fit to the BV equation remains a more accurate method.

We also observed a decrease of i_{lim} upon addition of more supporting salt $NaClO_4$. Such deviations of i_{lim} from conventional theory have been predicted to occur at low supporting electrolyte concentrations[37] and have been reported in several experiments with nanoelectrodes.[13,16,38,39] Several underlying mechanisms have been invoked to explain the observations including ion pairing,[40,41] adsorption of the redox species,[42] the Frumkin effect,[12,13] and electrolyte depletion,[21] but a general consensus has yet to emerge. We briefly address the relevance of these proposed mechanisms to our experimental situation.

Ion Pairing. It was shown by Watkins and White[12] that ion pairing between redox species and supporting electrolyte can lead to significant departures from ideal Butler–Volmer kinetics when the rate of mass transport is sufficiently high. The redox species employed here is neutral in the reduced state and monovalent in the oxidized state, however, and we do not expect ion pairing to play significant role in this case. We, however, note that redox cycling could provide an additional means of studying pairing kinetics because the potential at one electrode can influence the ratio of paired and unpaired molecules at the other electrode.

Electrolyte Depletion. Sun and Mirkin[21] recently reported a decreasing i_{lim} with decreasing concentration of KNO_3 in nanometer-sized cavities. They attributed this effect to depletion of ions from the bulk of their ultrasmall volume occasioned by the formation of the double layers at the electrodes. We can rule out this effect here, however, because in our experiments additional supporting electrolyte can diffuse into the device via the access holes so as to maintain a constant bulk concentration in the steady state.

Double-Layer Effects and Adsorption. At nanoelectrodes, an additional level of complexity is introduced because the size of the electrical double layer (i.e., the Debye length) can become comparable to the size of the diffusion layer. Significant departures from classic behavior have been reported with nanoelectrodes,[13,38,39] but detailed understanding is still lacking. The same considerations apply to our geometry, with the electrode spacing z replacing the nanoelectrode radius a as the relevant length scale. Because in the present measurements the Debye length λ is <1 nm and thus much smaller than z,

however, we do not expect these considerations to play a large role here. The heterogeneous rate constant k^0 also depends on the structure of the double layer via the Frumkin effect, which describes the influence on the apparent k^0 by the electrostatic potential at the outer Helmholtz plane, and thus represents an apparent rate constant. Our observation of a higher k^0 at higher KCl concentration appears consistent with the Frumkin effect for a negatively charged Pt electrode, consistent with previous observations.[12] The significantly lower rates observed when using $NaClO_4$ as supporting electrolyte, as well as the decrease of the rate at higher $NaClO_4$ concentration, do not, however, fit this simple electrostatic picture and instead point to ion-specific contributions at the electrode surface as being the dominant source of variations.

The experiments discussed here have focused on $Fc(MeOH)_2$, which is believed to undergo outer-sphere reduction and oxidation reactions and thus represents a chemically reversible redox system. Molecules with a propensity to irreversibly adsorb on the electrode or that are unstable in either their reduced or oxidized form may, however, prove particularly difficult to analyze with the present approach. This is because the electrodes, by virtue of being embedded inside a fluidic channel, cannot be repeatedly polished by mechanical means like a conventional UME. This limitation may, however, be at least partly mitigated by the compatibility of the devices with harsh chemical cleaning treatments.

Conclusion

Nanofluidic electrochemical devices based on redox cycling represent a major extension of the capabilities of thin-layer cells and can be routinely exploited for the determination of very fast electron-transfer rates ($k^0 > 1$ cm/s). The systematic fabrication approach, combined with the relatively large electrode surface area, allows a detailed characterization of the device geometry and its surface properties. Furthermore, while specialized equipment is required for fabrication, the completed devices are mechanically robust, can be stored for extended periods of time, and can be operated with standard potentiostats. In the future the electrode spacing can be further reduced to yield even more efficient mass transport. We thus envision nanofluidic devices becoming a widespread component in electrochemical sensors and a versatile tool that nicely complements SECM in a wide range of fundamental electrochemical experiments.

Supporting Information Available: Finite element calculations of the diffusion-limited current and a detailed characterization of the electrode surface by AFM, EDS, XPS, and cyclic voltammetry in sulfuric acid. This material is available free of charge via the Internet at http://pubs.acs.org.

JA902331U

(37) Oldham, K. B.; Bond, A. M. *J. Electroanal. Chem.* **2001**, *508*, 28–40.
(38) Conyers, J. L.; White, H. S. *Anal. Chem.* **2000**, *72*, 4441–4446.
(39) Krapf, D.; Quinn, B. M.; Wu, M. Y.; Zandbergen, H. W.; Dekker, C.; Lemay, S. G. *Nano Lett.* **2006**, *6*, 2531–2535.
(40) Beriet, C.; Pletcher, D. *J. Electroanal. Chem.* **1994**, *375*, 213–218.
(41) Watkins, J. J.; White, H. S. *J. Electroanal. Chem.* **2005**, *582*, 57–63.
(42) Beriet, C.; Pletcher, D. *J. Electroanal. Chem.* **1993**, *361*, 93–101.